Electronic, spintronic, and piezoelectric properties of new Janus ZnAXY (A = Si, Ge, Sn, and X, Y = S, Se, Te) monolayers

Nayereh Ghobadi,[1] Somayeh Gholami Rudi,[2] and Samaneh Soleimani-Amiri[3,*]
[1]*Department of Electrical Engineering, University of Zanjan, Zanjan, Iran*
[2]*Department of Electrical Engineering, Qaemshahr Branch, Islamic Azad University, Qaemshahr, Iran*
[3]*Faculty of Electrical and Computer Engineering, Babol Noshirvani University of Technology, Babol, 484, Iran*

(Received 18 August 2022; revised 20 December 2022; accepted 14 February 2023; published 28 February 2023)

Two-dimensional (2D) Janus materials due to their asymmetric structures show fascinating spintronic and piezoelectric properties making them a research hot spot in recent years. In this work, inspired by Janus group-III monochalcogenides, we propose ZnAXY (A = Si, Ge, Sn, and X/Y = S, Se, Te, $X < Y$) monolayers as a novel structure with broken inversion and mirror symmetry. By calculating cohesive energy and phonon dispersion, eight of nine possible ZnAXY monolayers are proved to be dynamically stable. In addition, thermal stability of these eight structures is confirmed by *ab initio* molecular dynamics simulations. The electronic band structures of ZnAXY monolayers indicate that all of them are indirect semiconductors with strong spin-orbit coupling effects. Lack of inversion symmetry gives rise to Zeeman-type spin splitting at the K point of the conduction band with the highest value of 136 meV for ZnSiSeTe. Furthermore, out-of-plane asymmetry results in Rashba spin splitting (RSS) at the Γ point of the valence and conduction bands in the most compositions of Janus ZnAXY monolayers. Among them, ZnGeSTe with $\alpha_R^{\Gamma_V}$ of 1.79 eV Å and $\alpha_R^{\Gamma_c}$ of 0.862 eV Å and ZnSiSTe with $\alpha_R^{\Gamma_V}$ of 1.537 eV Å and $\alpha_R^{\Gamma_c}$ of 0.756 eV Å are found to be great materials for future spintronic applications. Interestingly, in addition to large RSS, Mexican hat dispersion is observed at the Γ point of the topmost valence band in these materials. Moreover, the calculated elastic coefficients for the hexagonal ZnAXY monolayers confirm the mechanical stability of the predicted structures. Finally, Janus ZnAXY monolayers possess high in-plane (up to 7.46 pm/V) and out-of-plane (up to 0.67 pm/V) piezoelectric coefficients making them appealing alternatives for prevalent piezoelectric materials.

DOI: 10.1103/PhysRevB.107.075443

I. INTRODUCTION

After the successful synthesis of graphene in 2004 [1], two-dimensional (2D) materials have demonstrated a growing interest in different applications due to their intriguing properties and capabilities [2–5]. In the past decade, many experimental and theoretical researches have been trying to develop emerging 2D materials such as transition metal dichalcogenides (TMDs) [6–11], hexagonal boron nitride [12–15], 2D Xenes (e.g., phosphorene [16], silicene [17–20], etc.) and group-III monochalcogenides [21,22]. It is well-known that fascinating physical properties of 2D materials can be regulated by changing their atomic structures through chemical functionalization of surface atoms [23]. Surface functionalization strategies can be exploited to fabricate a new class of 2D materials with two different faces in their structures called Janus materials that has attracted burgeoning attention in recent years [24]. Research on 2D Janus materials began with theoretical calculations on hydrogenation and halogenation of graphene and its derivatives and the modified electronic, magnetic, and mechanical properties were explored [25–30]. In 2013, Zhang *et al.* for the first time experimentally realized a graphene-based Janus material by a two-step surface covalent functionalization and investigated its chemical reactivity and surface wettability of two sides [31]. Then, in 2017 the landmark synthesis of MoSSe as the first Janus TMD (JTMD) spurred a large amount of research in the field of 2D Janus materials [32,33]. Meanwhile, studies revealed that strong spin-orbit coupling (SOC) and mirror asymmetry in the atomic structure of 2D Janus materials give rise to Rashba spin splitting (RSS) phenomenon, endowing them with great potential for application in next generation spintronic devices. As an example, Hu *et al.* in 2018 systematically investigated the electronic band structures of different Janus TMD monolayers with chemical formula of MXY (M = Mo, W, and X/Y = S, Se, Te) [34]. They observed that similar to conventional TMDs, in all types of Janus TMDs Zeeman-type spin splitting and valley polarization at K (K') point exist due to the preserved in-plane asymmetry. In addition, in all MXY structures Rashba spin splitting appears around the Γ point as a result of broken out-of-plane mirror symmetry in Janus TMDs. In fact, different electronegativity of X and Y atoms builds an internal electric field perpendicular to the MXY plane and induces RSS in these polar systems [34]. As a more sophisticated Janus system, Patel *et al.* in 2022 proposed Janus TMD van der Waals heterostructures MoXY/WXY (X, Y = S, Se, Te; $X \neq Y$) and examined their band gaps and Rashba parameters using first-principles calculations [35]. Beyond

*Corresponding author: s.soleimani@nit.ac.ir

JTMDs, different Janus structures of group-III monochalcogenide monolayers $XMMY$, $XMM'X$ and $XMM'Y$ (M/M' = Ga or In and X/Y = S, Se, Te) with four sublayers were theoretically investigated and their stabilities were proven by first-principles method [36–40]. It was shown that Janus group-III monochalcogenides are semiconductors with band gaps in the range of 0.89–2.03 eV and in-plane piezoelectric coefficients four times higher than the maximum coefficient of their symmetric counterparts [37]. Moreover, a considerable optical absorption coefficient in the visible and near ultraviolet region is achieved for Janus M_2XY monolayers which render them as highly efficient photocatalytic materials [36]. Ju *et al.* in 2020 observed a remarkable Rashba spin splitting in Janus group-III monochalcogenide monolayers which could be manipulated by external electric field and biaxial strain and proposed these monolayers as promising materials for future spintronic applications [40]. Quite recently, Zhang *et al.* introduced ZnXY_2 (X = Si, Ge, Sn and Y = S, Se, Te) monolayers as a new class of Janus group-III monochalcogenides based on the similarity in atomic structure and number of valence electrons [41]. After investigating the stability of nine ZnXY_2 structures, they studied the mechanical, electronic, and piezoelectric properties of the seven monolayers where their stability was validated using first-principles calculations. It was shown that ZnXY_2 monolayers are wide direct band gap semiconductors with large effective mass difference between electrons and holes. They are also found to be flexible materials with higher in-plane piezoelectricity with respect to the conventional Janus group-III monochalcogenides and common piezoelectric materials. These fascinating properties represent ZnXY_2 structures as appropriate materials to be used in future optoelectronic applications, flexible devices, and electromechanical systems. The exciting properties of ZnXY_2 monolayers as well as the burgeoning need for new Janus 2D materials inspired us to propose ZnAXY (A = Si, Ge, Sn and X/Y = S, Se, Te, $X < Y$) monolayers as another type of Janus group-III monochalcogenides. Owing to the successful synthesis of ZnX and AY monolayers [42,43], it is reasonable to speculate the realization of ZnAXY through intercalating these monolayers. Having a large atomic size and electronegativity difference, the proposed ZnAXY structures are predicted to induce higher RSS effect and piezoelectricity in comparison with ZnXY_2 or conventional Janus group-III monochalcogenides. In this paper, we systematically investigate the stability, and structural, electronic, spintronic, and piezoelectric properties of Janus ZnAXY monolayers using first-principles calculations. After introducing the geometry of proposed structure, cohesive energy, phonon dispersion and *ab initio* molecular dynamics (AIMD) are calculated to validate the stability of ZnAXY monolayers. For the eight stable monolayers, the structural parameters after relaxation are obtained. Then, important electrical features such as charge transfer, electrostatic potential energy distribution, dipole moment, electronic band structure, and partial density of states (PDOS) are investigated. Our results show that all the eight stable ZnAXY monolayers are semiconductors with indirect band gap ranging from 0.59 to 1.43 eV. In addition, similar to other Janus materials, ZnAXY monolayers exhibit distinct spin splitting in their band structures. The extracted values for Zeeman spin splitting coefficients at the K point of the valence band and Rashba coefficients at the Γ point of the valence and conduction bands indicate strong spin-related properties in some ZnAXY monolayers making them fascinating materials for valleytronic and spintronic devices. Lastly, in-plane and out-of-plane piezoelectric coefficients are calculated and compared with fashionable bulk piezoelectric materials and 2D Janus structures. The remarkably higher out-of-plane piezoelectric coefficients in some ZnAXY monolayers pave the way for fabricating more sensitive and controllable nanoscale piezoelectric devices.

II. COMPUTATIONAL METHODS

In this paper, all simulations are carried out using SIESTA simulation package [44,45] based on density functional theory (DFT). For the exchange-correlation potential, the generalized gradient approximation with Perdew-Burke-Ernzerhof [46] is employed. For energy band calculations, fully relativistic pseudopotentials are adopted and the SOC effect is also taken into account. The maximum cutoff energy is set to be 200 Ry and a double-ζ plus polarization basis set is considered. The convergence criterion on the total energy is 10^{-6} eV and the geometries are fully relaxed until the Hellman-Feynman force on each atom becomes less than 0.01 eV Å^{-1}. A Monkhorst-Pack k point grid of $15 \times 15 \times 1$ is utilized to integrate over the first Brillouin zone. A large enough vacuum region (> 20 Å) is set to avoid interlayer Coulomb interaction in the normal direction. The AIMD simulation is carried out using the canonical ensemble (NVT) and Nosé-Hoover thermostat at 300 K for 6 ps (with time step of 4 fs) on a $5 \times 5 \times 1$ supercell to investigate the thermal stability of the proposed monolayers. The relaxed-ion elastic constants are computed using the finite difference method by the stress arising from a small applied strain [47]. Lastly, piezoelectric tensors are obtained by the geometric Berry phase approach in which the electronic contribution to the polarization along a chosen direction is calculated through the following equation [48]:

$$P_{e,\parallel} = \frac{if q_e}{8\pi^3} \int_A d\mathrm{k}_\perp \sum_{n=1}^{M} \int_0^{|G_\parallel|} dk_\parallel \left\langle u_{\mathrm{k}n} \middle| \frac{\delta}{\delta k_\parallel} \middle| u_{\mathrm{k}n} \right\rangle, \quad (1)$$

where f is the occupation number of states in the valence band, q_e is the charge of electron, M is the number of occupied bands, $u_{\mathrm{k}n}$ are the periodic Bloch functions, and $G_\parallel$ is the shortest reciprocal lattice vector along the given direction.

III. RESULTS AND DISCUSSION

A. Structural parameters and stability

Figure 1 illustrates the geometric structure of Janus ZnAXY (A = Si, Ge, Sn, and X/Y = S, Se, Te, $X < Y$) monolayers with four sublayers X-Zn-$A-Y$ which is similar to the atomic structure of Janus group-III monochalcogenides [40]. In these monolayers, Zn atom is sandwiched between one chalcogen atom (X) on one side and two atoms on the other side consisting of one group IV (A) and one chalcogen (Y). It should be noted that in all structures the chalcogen (X) connected to Zn is smaller than the chalcogen (Y) connected to A as schematically shown in Fig. 1(b).

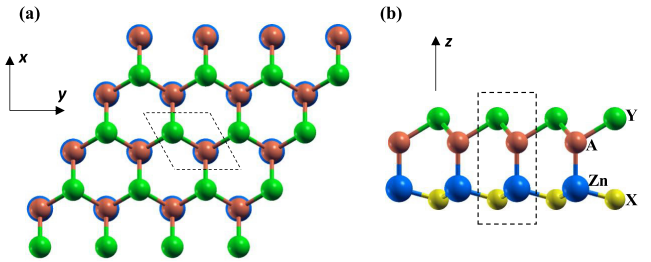

FIG. 1. (a) Top and (b) side views of the proposed Janus ZnAXY monolayer. The unit cell is displayed by the dashed lines.

The structural parameters obtained after relaxation are summarized in Table I. By inspecting the lattice constants (a), it can be seen that ZnSnSeTe, which is the heaviest structure, possesses the largest value of 4.207 Å. It is also observed that among ZnAXY structures with fixed A atom (Si, Ge, or Sn), the largest lattice constant belongs to ZnASeTe, which contains chalcogens with the largest atomic radius. On the other hand, the lightest structure (ZnSiSSe) owns the smallest lattice constant of 3.814 Å. Moreover, increasing the atomic radius of A (Si $\rightarrow$ Sn), $d_{\mathrm{Zn}-X}$, d_{A-Y}, $d_{\mathrm{Zn}-A}$ and the total thickness of the monolayer increase due to the decreased attractive force of the A atom in the structure. The stability of the studied structures is investigated by calculating cohesive energy (E_{coh}) through the following equation [49]:

$$E_{\mathrm{coh}} = \frac{E_{\mathrm{total}} - (E_{\mathrm{Zn}} + E_A + E_X + E_Y)}{N}, \qquad (2)$$

where E_{total} is the total energy of the Janus ZnAXY monolayer, E_{Zn}, E_A, E_X and E_Y are energies of isolated Zn, A, X, and Y atoms, respectively, and N is the number of atoms in the unit cell. The negative values of cohesive energy indicate that ZnAXY monolayers are energetically stable. Our calculation results show that ZnSiSSe is the most stable structure due to its smallest E_{coh} of −4.403 eV/atom (Table I). As can be seen, E_{coh} of all structures are lower than the experimentally fabricated MoS_2 (−2.63 eV/atom) and MoSSe (−2.34 eV/atom) [50], which ensures stability of the proposed structures.

As an accurate method to check the dynamic stability, the phonon dispersion calculations have been carried out for the proposed Janus ZnAXY monolayers and the results are depicted in Fig. 2. Absence of negative frequency in the Brillouin zone confirms the dynamic stability of the eight studied structures. We also examine the thermal stability of these eight monolayers through AIMD simulation at 300 K lasting for 6 ps with 1500 steps of 4 fs. Figure 3 shows the total energy fluctuation ($\Delta E\%$) and the inset illustrates the optimized structures before and after heating at 300 K. The small fluctuations of total energy together with the robustness of the structures during the whole heating period confirm the thermal stability of all ZnAXY monolayers. Nevertheless, a moderate ascending trend in the energy fluctuation graph and a slight deformation of the heated structure make ZnSiSSe relatively less thermally stable compared to the other ZnAXY monolayers. In addition to the results of cohesive energy, phonon dispersion, and AIMD calculations, which validated the stability of the proposed structures, the earlier synthesis of ZnX and AY sublayers is a strong proof of the fabrication feasibility of ZnAXY monolayers [42,43,51–53].

B. Electronic and spintronic properties

Lack of mirror symmetry in Janus 2D materials results in some fascinating polarization-dependent properties. For example, different electronegativities of lower and upper atoms in the ZnAXY monolayer induce an internal electric field and charge transfer between atoms which can be understood by Bader charge population analysis (Table II). Negative values in Table II represent electron loss of corresponding atoms while positive values show electron accumulation around them. As expected, in all structures charges transfer from Zn and A atoms to their connected chalcogens (X and Y) due to the larger electronegativity of the chalcogen family. Since the amount of charge transfer from Zn to X is different from A to Y, a nonzero out-of-plane electric field emerges in ZnAXY structures. This internal electric field can be confirmed by the electrostatic potential distributions illustrated in Fig. 4. Work functions at X and Y surfaces of the studied structures are accompanied by their dipole moments as the parameters showing the polarization effect in asymmetric Janus structures are listed in Table III. The work function difference between X and Y atoms (see $\Delta\phi$ in Fig. 4) is proportional to the dipole moment of the structures. The largest $\Delta\phi$ (2.186 eV) and dipole moment (0.721 Debye) belong to the ZnSiSSe monolayer, whereas ZnSnSTe possesses the smallest $\Delta\phi$ and dipole moment (0.749 eV and 0.346 debye). The sharper slope of the potential energy diagram at the X side compared to the Y side (Fig. 4) indicates that the internal electric field from Zn to X is stronger than from A to Y, which is in agreement with the results of Bader charge transfer analysis in Table II. This

TABLE I. The lattice constant (a), Zn-X bond length ($d_{\mathrm{Zn}-X}$), A-Y bond length (d_{A-Y}), Zn-A bond length ($d_{\mathrm{Zn}-A}$), thickness, and cohesive energy (E_{coh}) of the studied structures.

	a (Å)	$d_{\mathrm{Zn}-X}$ (Å)	d_{A-Y} (Å)	$d_{\mathrm{Zn}-A}$ (Å)	Thickness (Å)	E_{coh} (eV/atom)
ZnSiSSe	3.814	2.282	2.567	2.568	4.494	−4.403
ZnSiSTe	4.018	2.346	2.849	2.642	4.662	−3.92
ZnSiSeTe	4.123	2.449	2.875	2.541	4.74	−3.763
ZnGeSSe	3.865	2.284	2.622	2.707	4.582	−4.324
ZnGeSTe	4.047	2.351	2.888	2.783	4.759	−3.865
ZnGeSeTe	4.148	2.447	2.915	2.69	4.864	−3.709
ZnSnSTe	4.101	2.375	3.03	3.047	5.142	−3.758
ZnSnSeTe	4.207	2.464	3.057	2.934	5.218	−3.618

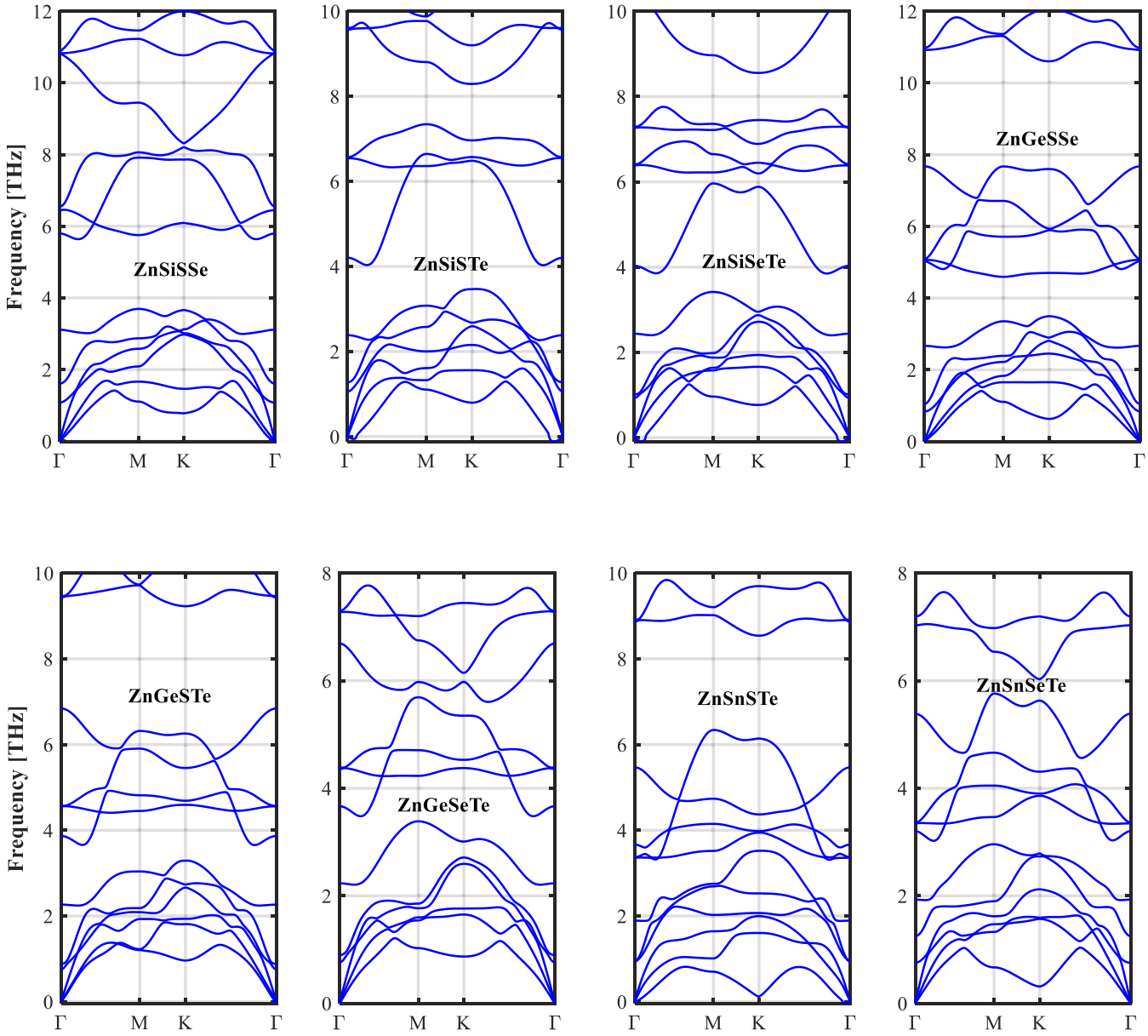

FIG. 2. The calculated phonon spectra of eight stable ZnAXY monolayers.

can be attributed to the higher electronegativity difference of Zn and X with respect to A and Y atoms.

In order to investigate the electronic properties of Janus ZnAXY monolayers, their band structures and partial densities of states (PDOSs) are calculated and shown in Fig. 5. As can be seen from the electronic band structures, all proposed ZnAXY monolayers are semiconductors with indirect band gaps. The smallest band gap of 0.54 eV belongs to ZnSiSeTe in which conduction band minimum (CBM) and valence band maximum (VBM) are located at M and Γ points, respectively. On the other hand, the ZnGeSTe possesses the largest band gap of 1.43 eV with the CBM between Γ and M points and VBM along the Γ-K path. To understand the contribution of each atom to the electronic states around the Fermi level, PDOSs of all monolayers are plotted next to their band structures in Fig. 5. By inspecting the PDOSs at the edge of the valence band it is found that in all structures p orbitals of chalcogen atoms (X and Y) are mainly responsible for the VBM. Moreover, comparing the shape of band structures around VBM, we observe Mexican-hat-like dispersion in the vicinity of Γ point of all structures except ZnSiSSe, ZnSiSeTe, and ZnSnSTe. Emergence of the Mexican hat in the topmost valence band moves the VBM from the Γ point to a point along the Γ-K path. The other peak of the Mexican hat occurs along the Γ-M direction which is negligibly lower (∼0.01 eV) than the VBM. Furthermore, Mexican hat dispersion induces a large Van Hove singularity in the PDOS at the energy slightly lower than the energy of VBM which corresponds to the Mexican hat's saddle point in the band structure. Considering the edge of the conduction band, CBM is mainly constructed of p orbitals of group IV atoms (A) and partly p orbitals of the chalcogens connected to A atoms (Y).

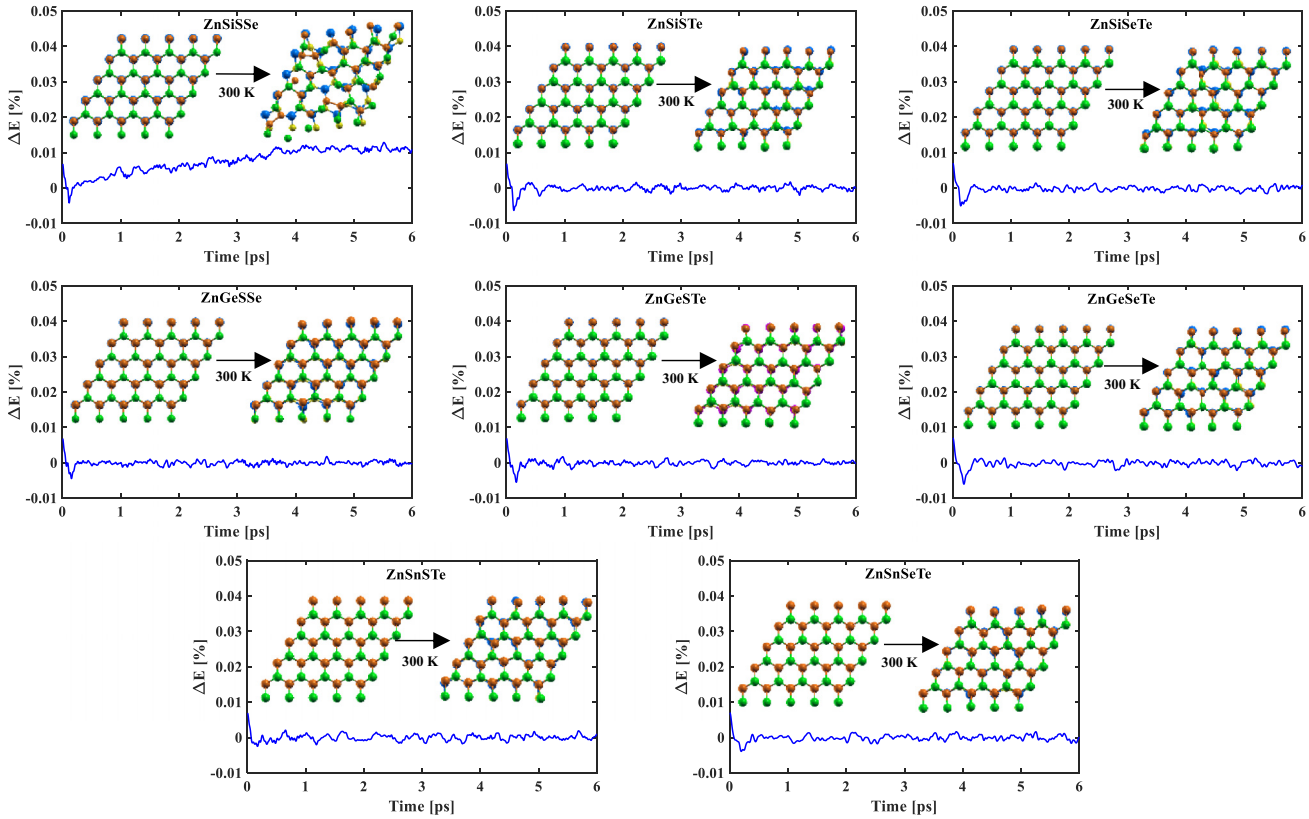

FIG. 3. The *ab initio* molecular dynamics (AIMD) simulation results at 300 K of ZnAXY monolayers. The inset shows the snapshots of $5 \times 5 \times 1$ supercells at 0 and 6 ps.

To explore the SOC effect in our Janus monolayers, the spin-related parameters are extracted from corresponding band structures and presented in Table IV. Moreover, to provide better insight into the Zeeman and Rashba type spin splitting, the related parameters are demonstrated in the band structure of ZnGeSTe and presented in Fig. 6. The first column of Table IV (λ_{K_c}) represents the magnitude of Zeeman spin splitting at the K point of the conduction band which has the highest values of 136 and 127 meV for ZnSiSeTe and ZnSiSTe monolayers, respectively. This valley dependent spin splitting is the result of inversion asymmetry in ZnAXY monolayers. Moreover, strong out-of-plane asymmetry in Janus ZnAXY structures leads to distinct Rashba spin splitting in their band structures. The Rashba coefficient, an important parameter to determine the strength of RSS, is defined by $\alpha_R = 2E_R/K_R$ where E_R and K_R are Rashba energy and momentum offset, respectively (see Fig. 6) [54,55]. Looking at the Rashba coefficients at the Γ point of the valence band it is found that except ZnSiSSe, ZnSiSeTe, and ZnSnSTe, the other five monolayers have considerable Rashba spin splittings. The values of 1.79 eV Å and 1.537 eV Å as $\alpha_R^{\Gamma_V}$ for ZnGeSTe and ZnSiSTe are much higher than the Rashba coefficients reported for most Janus TMDs [56]. It is worth noting that the existence of both large RSS and Mexican-hat dispersion at the Γ point of the topmost valence band of these five structures (Fig. 5) makes them good candidates for future spintronic applications. Considering the Rashba coefficients at the Γ

TABLE II. The results of Bader charge population analysis of Janus ZnAXY monolayers.

	X (e)	Zn (e)	A (e)	Y (e)
ZnSiSSe	0.811	−0.831	−0.636	0.656
ZnSiSTe	0.85	−0.824	−0.428	0.402
ZnSiSeTe	0.685	−0.67	−0.388	0.373
ZnGeSSe	0.846	−0.774	−0.716	0.644
ZnGeSTe	0.86	−0.81	−0.483	0.432
ZnGeSeTe	0.71	−0.697	−0.44	0.427
ZnSnSTe	0.871	−0.824	−1.879	1.831
ZnSnSeTe	0.744	−0.662	−0.798	0.717

TABLE III. The Work functions of X and Y atomic surfaces (ϕ_X and ϕ_Y) and dipole moments (μ) of the studied Janus ZnAXY structures.

	ϕ_X (eV)	ϕ_Y (eV)	μ (Debye)
ZnSiSSe	6.047	3.861	0.721
ZnSiSTe	5.391	3.274	0.656
ZnSiSeTe	5.283	3.307	0.694
ZnGeSSe	5.609	4.312	0.482
ZnGeSTe	4.813	3.544	0.436
ZnGeSeTe	5.072	3.742	0.516
ZnSnSTe	4.634	3.885	0.346
ZnSnSeTe	5.042	4.062	0.463

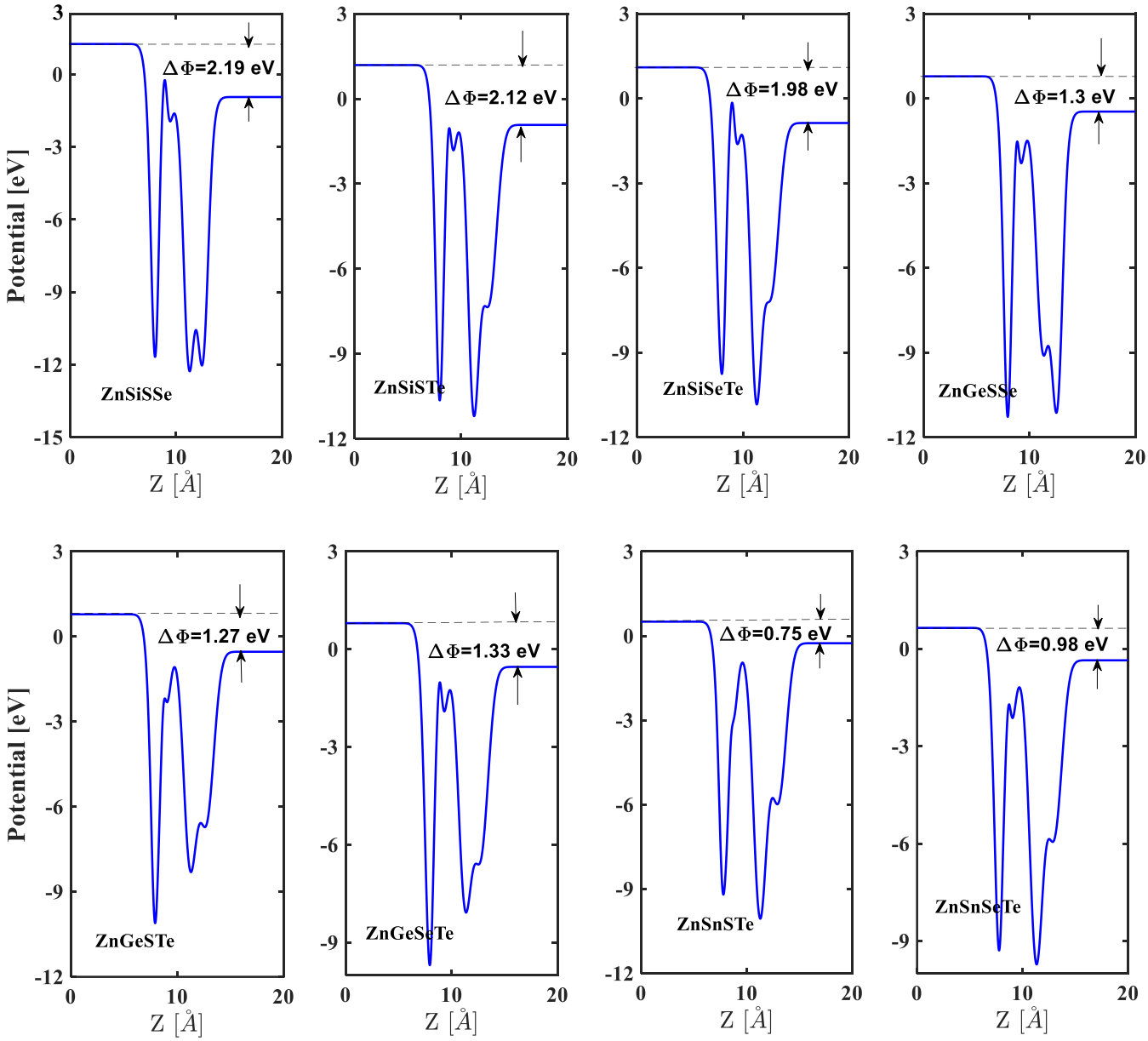

FIG. 4. The electrostatic potential energy of Janus ZnAXY monolayers along the z direction. The values of work function difference $\Delta\phi$ are inserted inside the figures.

point of the lowest conduction band ($\alpha_R^{\Gamma c}$) in Table IV, it can be seen that six structures possess nonzero coefficients while ZnSiSSe and ZnGeSSe do not experience RSS at this point, which is consistent with their band structures shown in Fig. 5. Close scrutiny of the first and second conduction bands around the M point reveals small RSS in all structures, especially in monolayers containing a Te atom. Finally, it should be mentioned that since the proposed Janus structures do not have heavy transition metals (e.g., Mo and W) in their compounds, the observed Rashba effect is mostly originated from the broken out-of-plane symmetry in these monolayers.

For better comprehension of spin-related phenomena such as Rashba and Zeeman spin splittings, plots of spin texture for ZnGeSTe in the first Brillouin Zone are given in Fig. 7. The plots are drawn in the K_x-K_y plane centered at Γ point for the first and second valence and conduction bands. In these plots, the black arrows and colored contours indicate the in-plane ($S_x(k)$, $S_y(k)$) and out-of-plane ($S_z(k)$) spin polarization vectors, respectively. In Figs. 7(a) and 7(b), the clockwise and counterclockwise rotation of arrows around the Γ point of first and second valence bands with no out-of-plane spin polarization component ($S_z(k)$) prove RSS characteristics in the ZnGeSTe valence band. This result is in agreement with the large value of $\alpha_R^{\Gamma v}$ (1.79 eV Å) for ZnGeSTe reported in Table IV. In the same way, it can be inferred from Figs. 7(c) and 7(d) that there is a strong RSS around the Γ point and a weak RSS around the M point of the first and second conduction bands in ZnGeSTe monolayer. Finally, the dark blue and red contours at the K point of the first and second conduction bands imply opposite spin polarization, which corresponds to

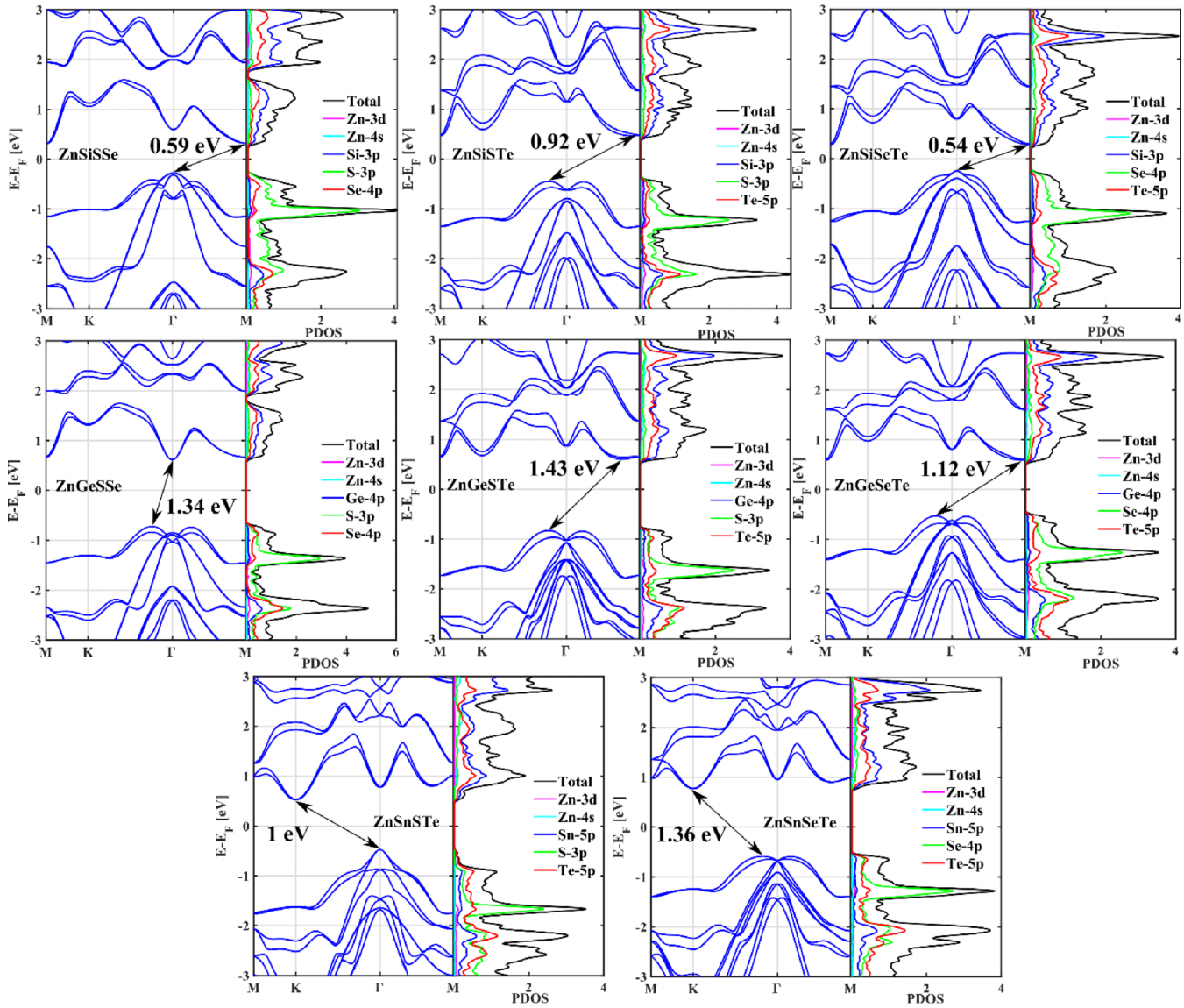

FIG. 5. The band structures of Janus ZnAXY monolayers along with their partial density of states (PDOS).

the Zeeman spin splitting observed in the band structure of ZnGeSTe.

In order to delve deep into the electronic and spintronic properties of ZnAXY monolayers, the spatial charge density distributions of ZnSnSTe and ZnSnSeTe at Γ and K points of the lower conduction band (LCB) and the Γ point of the upper valence band (UVB) are visualized in Fig. 8. The charge density distribution at the Γ point of LCB shows a highly localized charge density at Zn and its connected chalcogen (S or Se) of ZnSnSTe and ZnSnSeTe monolayers which is a result of their structural asymmetry. Considering the side view of charge density distribution at the K valley of LCB, it is observed that in contrast to the Γ point the charge is distributed around Sn and Te atoms in both ZnSnSTe and ZnSnSeTe structures, while there is no charge density around Zn and its connected chalcogen. Furthermore, it is obvious from the top view of charge density plots of LCB at the K point that charge density is delocalized and expanded between Sn and Te atoms in ZnSnSTe and ZnSnSeTe monolayers. The similar behavior of charge distribution in the LCB of ZnSnSTe and ZnSnSeTe coincides with the nearly equal values of λ_{K_C} and $\alpha_R^{\Gamma_C}$ in Table IV for these two materials. Lastly, at the Γ point of UVB in ZnSnSTe the charge density is distributed

TABLE IV. The spin splitting at the K point of conduction band (λ_{K_C}), the Rashba coefficient at the Γ point of valence band ($\alpha_R^{\Gamma_V}$) and Γ point of conduction band ($\alpha_R^{\Gamma_C}$).

	λ_{K_C} (meV)	$\alpha_R^{\Gamma_V}$ (eV Å)	$\alpha_R^{\Gamma_C}$ (eV Å)
ZnSiSSe	68	0.0	0.0
ZnSiSTe	127	1.537	0.756
ZnSiSeTe	136	0.0	0.309
ZnGeSSe	17	0.927	0.0
ZnGeSTe	77	1.79	0.862
ZnGeSeTe	85	0.926	0.335
ZnSnSTe	11	0.0	0.399
ZnSnSeTe	3	0.993	0.342

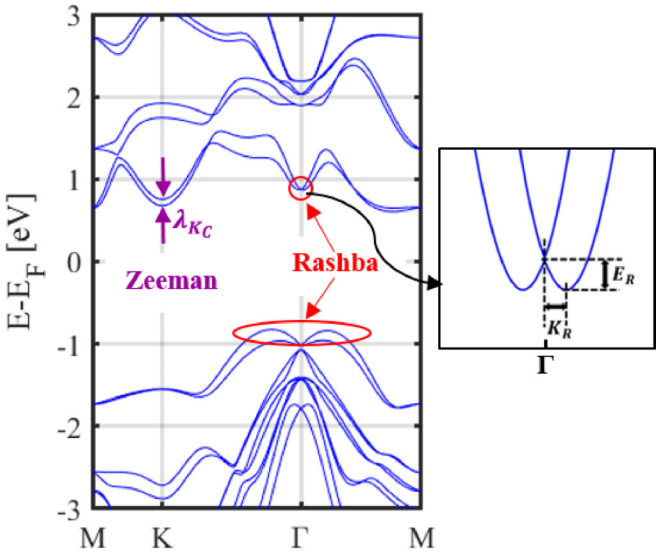

FIG. 6. The band structure of Janus ZnGeSTe monolayer with specified Zeeman and Rashba spin splittings. The Rashba energy (E_R) and momentum offset (K_R) are indicated in the magnified window.

along the bonds between Sn and Te while in ZnSnSeTe is localized at Sn, Se, and Te atoms. These different charge distributions are compatible with largely different values of $\alpha_R^{\Gamma_V}$ in ZnSnSTe and ZnSnSeTe monolayers.

C. Piezoelectric properties

Due to the lack of centrosymmetry and out-of-plane mirror symmetry, the proposed Janus ZnAXY structures are highly expected to show piezoelectric effect. The piezoelectric coefficient of 2D piezoelectric materials (d_{ij}) is related to the elastic tensor (C_{jk}) and the piezoelectric tensor (e_{ik}) through the following equation [41]:

$$e_{ik} = d_{ij}C_{jk}, \tag{3}$$

where the piezoelectric tensor and coefficient for ZnAXY with *P3m1* point group symmetry can be expressed as

$$e_{ij} = \begin{pmatrix} -e_{11} & e_{11} & 0 & e_{15} & 0 & 0 \\ 0 & 0 & 0 & 0 & e_{15} & -e_{11} \\ e_{31} & e_{31} & e_{33} & 0 & 0 & 0 \end{pmatrix}, \tag{4}$$

$$d_{ij} = \begin{pmatrix} -d_{11} & d_{11} & 0 & d_{15} & 0 & 0 \\ 0 & 0 & 0 & 0 & d_{15} & -2d_{11} \\ d_{31} & d_{31} & d_{33} & 0 & 0 & 0 \end{pmatrix}, \tag{5}$$

where e_{11} and e_{31} represent in-plane and out-of-plane polarizations, respectively. In 2D materials, stresses and strains are only permitted within the basal plane [57], while the normal axis is strain/stress free (i.e., $\varepsilon_3 = \varepsilon_4 = \varepsilon_5 = 0$ and $\sigma_3 = \sigma_4 = \sigma_5 = 0$). Therefore, $e_{15}/d_{15} = 0$ and $e_{33}/d_{33} = 0$. Solving Eq. (3) using the above matrices results in in-plane (d_{11}) and out-of-plane (d_{31}) polarization coefficients:

$$d_{11} = \frac{e_{11}}{C_{11} - C_{12}}, \tag{6}$$

$$d_{31} = \frac{e_{31}}{C_{11} + C_{12}}, \tag{7}$$

where C_{11} and C_{12} stand for relaxed-ion elastic stiffness coefficients. The calculated elastic and piezoelectric coefficients for the proposed ZnAXY monolayers are listed in Table V. It can be seen that C_{11} ranges from 54.89 to 75.64 N/m and C_{12}

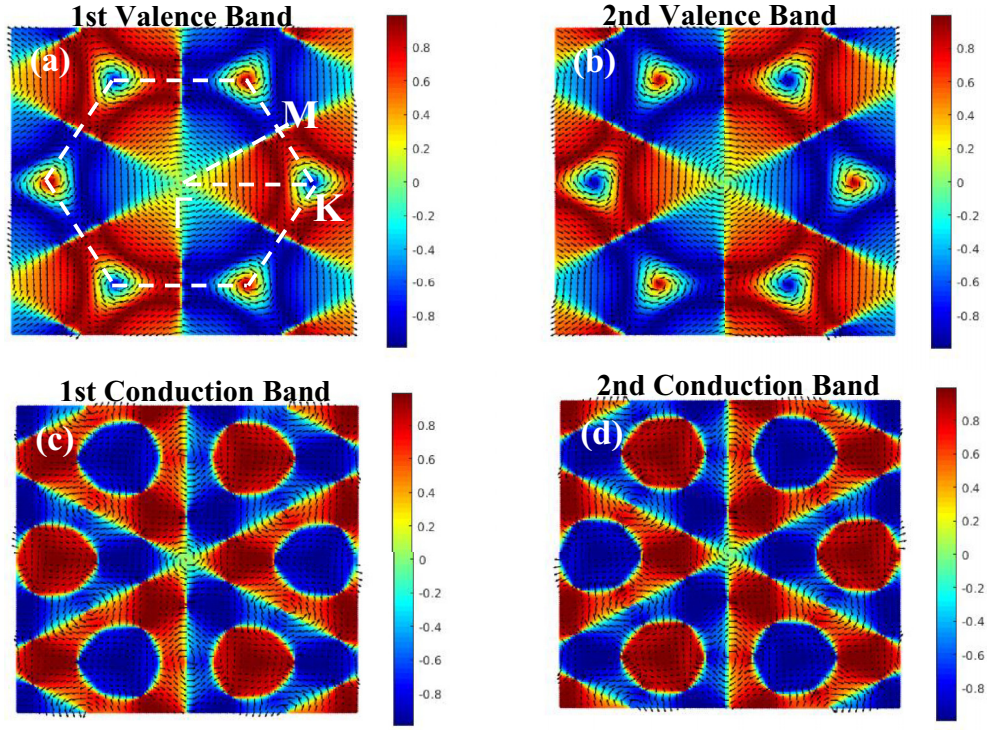

FIG. 7. Plots of spin texture for the first and second (a), (b) valence bands, and (c), (d) conduction bands of ZnGeSTe.

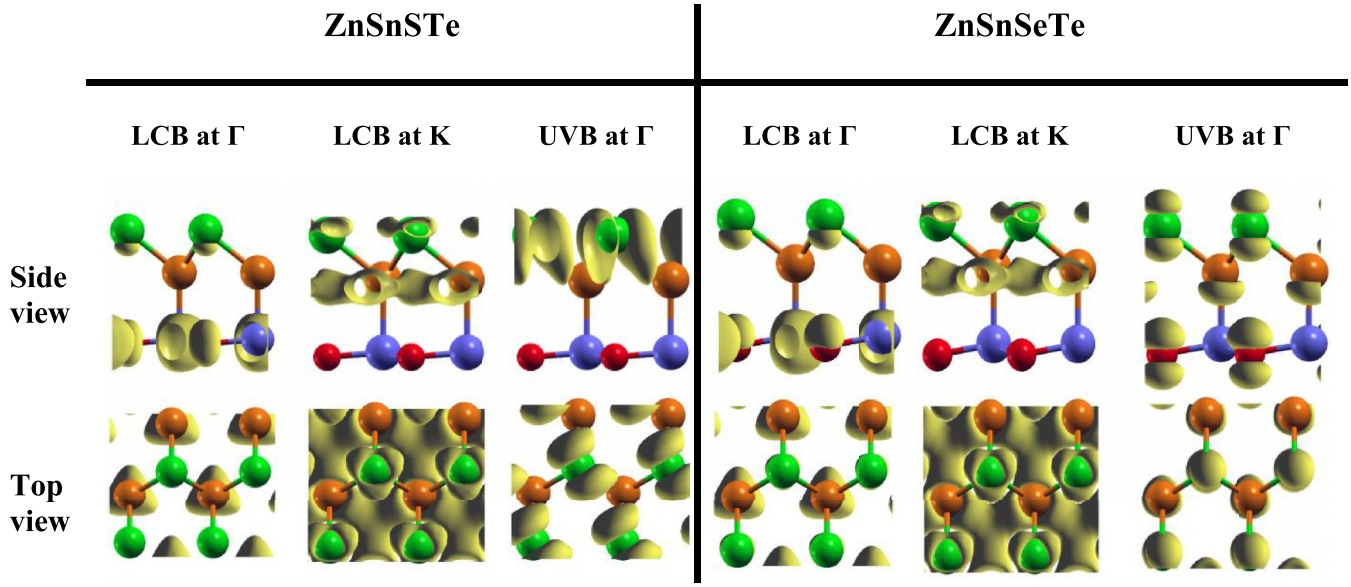

FIG. 8. Spatial charge density distributions of ZnSnSTe and ZnSnSeTe at the Γ- and K points of the lower conduction band (LCB), and the Γ point of the upper valence band (UVB).

from 16.48 to 27.56 N/m. It is well known that in hexagonal structures, $C_{11} > |C_{12}|$ should be satisfied for mechanical stability [58]. As observed in Table V, for all monolayers C_{11} is larger than the corresponding C_{12}, which fulfills the mentioned mechanical criterion and proves that all proposed structures are mechanically stable. It can also be seen that the in-plane piezoelectric coefficient (d_{11}) is in the range of 2.37 to 7.46 pm/V. These values of d_{11} are in the same order or even higher than those of commercial bulk piezoelectric materials such as quartz (2.3 pm/V) [59], wurtzite-GaN (3.1 pm/V) [60], and wurtzite-AlN (5.1 pm/V) [60] and newly emerging 2D materials like MoS_2 (3.73 pm/V) [61], GaSe (2.30 pm/V) [62], MoSeTe (4.17 pm/V) [63], and Janus group-III monochalcogenides (1.91–8.47 pm/V) [37,64]. As can be seen in Table V, broken out-of-plane symmetry in Janus ZnAXY leads to nonzero values of e_{31} and d_{31}. The minus sign of the out-of-plane piezoelectric coefficient shows the direction of polarization. Comparing d_{31} and d_{11} values, it is observed that out-of-plane piezoelectric coefficients are about one order of magnitude smaller than in-plane coefficients. Further inspection of Table V reveals that in ZnAXY structures with the same A atom, e_{11} and e_{31} decrease when the atomic size of constituents increases. This trend can be attributed to the decrease of the electronegativity difference between Zn (A) and X (Y) atoms ($|\Delta\boldsymbol{\gamma}_{\mathrm{Zn}-X}|$ and $|\Delta\boldsymbol{\gamma}_{A-Y}|$), which leads less asymmetric charge distribution and consequently smaller piezoelectricity [41]. Moreover, our results show that piezoelectricity is also dependent on interatomic distance between Zn (A) and X (Y) atoms (see $d_{\mathrm{Zn}-X}$ and d_{A-Y} in Table I) and larger distances correspond to smaller piezoelectric coefficients. It is worth noting that there are limited 2D materials that possess a nonzero out-of-plane piezoelectric coefficient [41,65,66] and our observed d_{31} for ZnAXY monolayers can be of great importance. Besides, as shown in Table V, d_{31} ranges from 0.32 to 0.67 pm/V, which is higher than the reported values for Janus group-III monochalcogenides (0.07–0.46 pm/V) [63], Janus transition metal dichalcogenide monolayers (0.004–0.41 pm/V) [63,67], and ZnXY_2 (0.2−0.58 pm/V) [41]. The large values of d_{31} for ZnSiSSe (0.66 pm/V) and ZnGeSSe (0.67 pm/V) make them promising materials to be used in flexible piezoelectric devices and increase the compatibility with current microelectronic technologies which consist of vertically stacked functional layers.

TABLE V. The calculated relaxed-ion elastic stiffness coefficients (C_{11} and C_{12}) and piezoelectric coefficients (e_{11}, e_{31}, d_{11}, and d_{31}) of Janus ZnAXY monolayers and the electronegativity differences between Zn (A) and X (Y) atoms ($|\Delta\boldsymbol{\gamma}_{\mathrm{Zn}-X}|$ and $|\Delta\boldsymbol{\gamma}_{A-Y}|$)

	C_{11} (N/m)	C_{12} (N/m)	e_{11} (10^{-10} C/m)	e_{31} (10^{-10} C/m)	d_{11} (pm/V)	d_{31} (pm/V)	$\lvert\Delta\boldsymbol{\gamma}_{\mathrm{Zn}-X}\rvert$	$\lvert\Delta\boldsymbol{\gamma}_{A-Y}\rvert$
ZnSiSSe	60.84	16.48	3.31	−0.51	7.46	−0.66	0.93	0.65
ZnSiSTe	69.37	22.01	1.46	−0.41	3.08	−0.45	0.93	0.2
ZnSiSeTe	54.89	20.84	1.11	−0.29	3.26	−0.38	0.9	0.2
ZnGeSSe	66.44	27.56	2.35	−0.63	6.04	−0.67	0.93	0.54
ZnGeSTe	75.64	24.92	1.2	−0.38	2.37	−0.38	0.93	0.09
ZnGeSeTe	60.61	22.47	1.06	−0.32	2.78	−0.39	0.9	0.09
ZnSnSTe	69.67	22.63	1.18	−0.35	2.51	−0.38	0.93	0.14
ZnSnSeTe	68.82	21.31	1.16	−0.29	2.44	−0.32	0.9	0.14

IV. CONCLUSIONS

In this paper, we studied the structural, electronic, spintronic, and piezoelectric properties of 2D Janus ZnAXY (A = Si, Ge, Sn, and X/Y = S, Se, Te, $X < Y$) monolayers using first-principles calculations. In order to validate the stability of the proposed structures, cohesive energies, phonon dispersions, and AIMD were calculated and the results revealed that all possible ZnAXY monolayers except ZnSnSSe are dynamically stable. Lack of out-of-plane symmetry in Janus ZnAXY structures leads to various polarization-related effects such as non-zero internal electric field, dipole moment, and work function difference between X and Y surfaces. The calculated electronic band structures for the eight stable ZnAXY monolayers showed that all of them are semiconductors with indirect band gaps in the range of 0.59–1.43 eV. In terms of SOC effect, lack of inversion symmetry in ZnAXY monolayers results in Zeeman-type spin splitting at the K point of the conduction band which has the highest value of 136 meV for ZnSiSeTe. Moreover, broken out-of-plane symmetry gives rise to Rashba spin splittings at the Γ point of valence and conduction bands. The large Rashba coefficient (1.79 eV Å) observed in the proposed ZnGeSTe is much higher than the largest Rashba coefficients reported for Janus TMDs. The spin texture plots in the first Brillouin zone of first and second conduction and valence bands for ZnGeSTe were demonstrated and the opposite rotation of arrows around the Γ point along with zero out-of-plane spin polarization components confirmed the observed RSS at this point. Furthermore, large in-plane (2.37−7.46 pm/V) and out-of-plane piezoelectric coefficients (0.32-0.67 pm/V) are witnessed in ZnAXY monolayers due to the breaking of inversion and mirror symmetry. These coefficients are comparable to or higher than those of conventional bulk and 2D piezoelectric materials. In summary, great electronic, spintronic, and piezoelectric properties of the proposed Janus ZnAXY monolayers indicate that these structures have a promising prospect in the future for 2D sensors, actuators, and other electromechanical devices.

ACKNOWLEDGMENT

This research is funded by Babol Noshirvani University of Technology, research grant program No. P/M/1121.

[1] K. S. Novoselov, A. K. Geim, S. V. Morozov, D. Jiang, Y. Zhang, S. V. Dubonos, I. V. Grigorieva, and A. A. Firsov, Electric field effect in atomically thin carbon films, Science **306**, 666 (2004).

[2] G. R. Bhimanapati, Z. Lin, V. Meunier, Y. Jung, J. Cha, S. Das, D. Xiao *et al.*, Recent advances in two-dimensional materials beyond graphene, ACS nano **9**, 11509 (2015).

[3] K. Khan, A. K. Tareen, M. Aslam, R. Wang, Y. Zhang, A. Mahmood, Z. Ouyang, H. Zhang, and Z. Guo, Recent developments in emerging two-dimensional materials and their applications, J. Mater. Chem. C **8**, 387 (2020).

[4] S. G. Rudi, R. Faez, M. K. Moravvej-Farshi, and K. Saghafi, Effect of Stone-Wales defect on an armchair graphene nanoribbon-based photodetector, Superlattices Microstruct. **130**, 127 (2019).

[5] S. G. Rudi and S. Soleimani-Amiri, Bilayer armchair graphene nanoribbon photodetector with Stone-Wales defect: A computational study, Mater. Sci. Semicond. Process. **150**, 106918 (2022).

[6] S. Manzeli, D. Ovchinnikov, D. Pasquier, O. V. Yazyev, and A. Kis, 2D transition metal dichalcogenides, Nature Rev. Mater. **2**, 17033 (2017).

[7] A. H. Castro Neto, Charge Density Wave, Superconductivity, and Anomalous Metallic Behavior in 2d Transition Metal Dichalcogenides, Phys. Rev. Lett. **86**, 4382 (2001).

[8] Z. Wei, B. Li, C. Xia, Y. Cui, J. He, J.-B. Xia, and J. Li, Various structures of 2D transition-metal dichalcogenides and their applications, Small Methods **2**, 1800094 (2018).

[9] S. Ahmed and J. Yi, Two-dimensional transition metal dichalcogenides and their charge carrier mobilities in field-effect transistors, Nano-Micro Lett. **9**, 1 (2017).

[10] S. Soleimani-Amiri and S. G. Rudi, Effects of sulfur line vacancy defects on the electronic and optical properties of armchair MoS_2 nanoribbon, Opt. Mater. **110**, 110491 (2020).

[11] S. G. Rudi and S. Soleimani-Amiri, Modulation of electronic and optical properties of line defected armchair MoS2 nanoribbon by vacancy passivation, J. Phys. Condens. Matter **33**, 185503 (2021).

[12] M. Hofmann, Y. C. Shin, Ya-Ping Hsieh, M. S. Dresselhaus, and J. Kong, A facile tool for the characterization of two-dimensional materials grown by chemical vapor deposition, Nano Res. **5**, 504 (2012).

[13] L. Song, L. Ci, H. Lu, P. B. Sorokin, C. Jin, J. Ni, A. G. Kvashnin, D. G. Kvashnin, J. Lou, B. I. Yakobson, and P. M. Ajayan, Large scale growth and characterization of atomic hexagonal boron nitride layers, Nano Lett. **10**, 3209 (2010).

[14] J. Zhang, B. Tan, X. Zhang, F. Gao, Y. Hu, L. Wang, X. Duan, Z. Yang, and P. Hu, Atomically thin hexagonal boron nitride and its heterostructures, Adv. Mater. **33**, 2000769 (2020).

[15] S. Yuan, C. Shen, B. Deng, X. Chen, Q. Guo, Y. Ma, A. Abbas, B. Liu, R. Haiges, C. Ott, T. Nilges, K. Watanabe, T. Taniguchi, O. Sinai, D. Naveh, C. Zhou, and F. Xia, Air-stable room-temperature mid-infrared photodetectors based on hBN/black arsenic phosphorus/hBN heterostructures, Nano Lett. **18**, 3172 (2018).

[16] A. Carvalho, M. Wang, Xi Zhu, A. S. Rodin, H. Su, and A. H. Castro Neto, Phosphorene: From theory to applications, Nat. Rev. Mater. **1**, 16061 (2016).

[17] S. Cahangirov, M. Topsakal, E. Aktürk, H. Şahin, and S. Ciraci, Two- and one-Dimensional Honeycomb Structures of Silicon and Germanium, Phys. Rev. Lett. **102**, 236804 (2009).

[18] H. Liu, J. Gao, and J. Zhao, Silicene on substrates: A way to preserve or tune its electronic properties, J. Phys. Chem. C **117**, 10353 (2013).

[19] T. P. Kaloni, N. Singh, and U. Schwingenschlögl, Prediction of a quantum anomalous hall state in co-decorated silicene, Phys. Rev. B **89**, 035409 (2014).

[20] A. Gooran-Shoorakchaly, A. A. Ahmadchally, S. Soleimani-Amiri, and M. Gholipour, Design of a low-power short-channel electrostatically doped silicene nanoribbon FET, IEEE Trans. Electron Devices **68**, 1956 (2021).

[21] S. Demirci, N. Avazlı, E. Durgun, and S. Cahangirov, Structural and electronic properties of monolayer group III monochalcogenides, Phys. Rev. B **95**, 115409 (2017).

[22] Y. Bai, Q. Zhang, N. Xu, K. Deng, and E. Kan, The Janus structures of group-III chalcogenide monolayers as promising photocatalysts for water splitting, Appl. Surf. Sci. **478**, 522 (2019).

[23] L. Zhang, Z. Yang, T. Gong, R. Pan, H. Wang, Z. Guo, H. Zhang, and X. Fu, Recent advances in emerging Janus two-dimensional materials: From fundamental physics to device applications, J. Mater. Chem. A **8**, 8813 (2020).

[24] V. Montes-García and P. Samorì, Janus 2D materials via asymmetric molecular functionalization, Chem. Sci. **13**, 315 (2022).

[25] W. Tao, N. Kong, X. Ji, Y. Zhang, A. Sharma, J. Ouyang, B. Qi *et al.*, Emerging two-dimensional monoelemental materials (Xenes) for biomedical applications, Chem. Soc. Rev. **48**, 2891 (2019).

[26] J. Zhou, Q. Wang, Q. Sun, X. S. Chen, Y. Kawazoe, and P. Jena, Ferromagnetism in semihydrogenated graphene sheet, Nano Lett. **9**, 3867 (2009).

[27] J. Zhou, M. M. Wu, X. Zhou, and Q. Sun, Tuning electronic and magnetic properties of graphene by surface modification, Appl. Phys. Lett. **95**, 103108 (2009).

[28] X. Li, S. Zhang, F. Q. Wang, Y. Guo, J. Liu, and Q. Wang, Tuning the electronic and mechanical properties of penta-graphene via hydrogenation and fluorination, Phys. Chem. Chem. Phys. **18**, 14191 (2016).

[29] R. Singh and G. Bester, Hydrofluorinated graphene: Two-dimensional analog of polyvinylidene fluoride, Phys. Rev. B **84**, 155427 (2011).

[30] M. Yang, R. Zhao, J. Wang, L. Zhang, Q. Xie, Z. Liu, and Z. Liu, Bandgap opening in Janus-type mosaic graphene, J. Appl. Phys. **113**, 084313 (2013).

[31] L. Zhang, J. Yu, M. Yang, Q. Xie, H. Peng, and Z. Liu, Janus graphene from asymmetric two-dimensional chemistry, Nat. Commun. **4**, 1443 (2013).

[32] A. Y. Lu, H. Zhu, J. Xiao, C. P. Chuu, Y. Han, M. H. Chiu, C. C. Cheng, C. W. Yang, K. H. Wei, Y. Yang, Y. Wang, D. Sokaras, D. Nordlund, P. Yang, D. A. Muller, M. Y. Chou, X. Zhang, and L. J. Li, Janus monolayers of transition metal dichalcogenides, Nat. Nanotechnol. **12**, 744 (2017).

[33] J. Zhang, S. Jia, I. Kholmanov, L. Dong, D. Er, W. Chen, H. Guo, Z. Jin, V. B. Shenoy, L. Shi, and J. Lou, Janus monolayer transition-metal dichalcogenides, ACS nano **11**, 8192 (2017).

[34] T. Hu, F. Jia, G. Zhao, J. Wu, A. Stroppa, and W. Ren, Intrinsic and anisotropic Rashba spin splitting in Janus transition-metal dichalcogenide monolayers, Phys. Rev. B **97**, 235404 (2018).

[35] S. Patel, U. Dey, N. P. Adhikari, and A. Taraphder, Electric field and strain-induced band-gap engineering and manipulation of the Rashba spin splitting in Janus van der Waals heterostructures, Phys. Rev. B **106**, 035125 (2022).

[36] A. Huang, W. Shi, and Z. Wang, Optical properties and photocatalytic applications of two-dimensional Janus group-III monochalcogenides, J. Phys. Chem. C **123**, 11388 (2019).

[37] Y. Guo, S. Zhou, Y. Bai, and J. Zhao, Enhanced piezoelectric effect in Janus group-III chalcogenide monolayers, Appl. Phys. Lett. **110**, 163102 (2017).

[38] A. Kandemir and H. Sahin, Janus single layers of In_2SSe: A first-principles study, Phys. Rev. B **97**, 155410 (2018).

[39] H. D. Bui, H. R. Jappor, and N. N. Hieu, Tunable optical and electronic properties of Janus monolayers Ga_2SSe, Ga_2STe, and Ga_2SeTe as promising candidates for ultraviolet photodetectors applications, Superlattices Microstruct. **125**, 1 (2019).

[40] W. Ju, D. Wang, T. Li, Y. Zhang, Z. Gao, L. Ren, H. Li, and S. Gong, Remarkable Rashba spin splitting induced by an asymmetrical internal electric field in polar III–VI chalcogenides, Phys. Chem. Chem. Phys. **22**, 9148 (2020).

[41] T. Zhang, Y. Liang, H. Guo, H. Fan, and X. Tian, The high piezoelectricity, flexibility and electronic properties of new Janus $ZnXY_2$ (X = Ge, Sn, Si and Y = S, Se, Te) monolayers: A first-principles research, Appl. Surf. Sci. **579**, 152017 (2022).

[42] S. P. Poudel and S. Barraza-Lopez, Metastable piezoelectric group-IV monochalcogenide monolayers with a buckled honeycomb structure, Phys. Rev. B **103**, 024107 (2021).

[43] X. Deng, D. C. Sorescu, and J. Lee, Single-layer ZnS supported on Au(111): A combined XPS, LEED, STM and DFT study, Surf. Sci. **658**, 9 (2017).

[44] J. M. Soler, E. Artacho, J. D. Gale, A. García, J. Junquera, P. Ordejón, and D. Sánchez-Portal, The SIESTA method for *ab initio* order-N materials simulation, J. Phys. Condens. Matter **14**, 2745 (2002).

[45] W. Kohn and L. J. Sham, Self-consistent equations including exchange and correlation effects, Phys. Rev. **140**, A1133 (1965).

[46] N. Troullier and José Luís Martins, Efficient pseudopotentials for plane-wave calculations, Phys. Rev. B **43**, 1993 (1991).

[47] X. Wu, D. Vanderbilt, and D. R. Hamann, Systematic treatment of displacements, strains, and electric fields in density-functional perturbation theory, Phys. Rev. B **72**, 035105 (2005).

[48] R. D. King-Smith and D. Vanderbilt, Theory of polarization of crystalline solids, Phys. Rev. B **47**, 1651 (1993).

[49] A. Rezavand, N. Ghobadi, and B. Behnamghader, Electronic and spintronic properties of Janus $MSi_2P_xAs_y$ (M = Mo, W) monolayers, Phys. Rev. B **106**, 035417 (2022).

[50] F. Li, W. Wei, Pei Zhao, B. Huang, and Y. Dai, Electronic and optical properties of pristine and vertical and lateral heterostructures of Janus MoSSe and WSSe, J. Phys. Chem. Lett. **8**, 5959 (2017).

[51] J. Wang, X. Yang, J. Cao, Y. Wang, and Q. Li, Computational study of the electronic, optical and photocatalytic properties of single-layer hexagonal zinc chalcogenides, Comput. Mater. Sci. **150**, 432 (2018).

[52] R. Chaurasiya, A. Dixit, and R. Pandey, Strain-driven thermodynamic stability and electronic transitions in ZnX (X = O, S, Se, and Te) monolayers, J. Appl. Phys. **125**, 082540 (2019).

[53] Y. Dai, X. Zhang, Y. Cui, M. Li, Y. Luo, F. Jiang, R. Zhao, and Y. Huang, Theoretical insights into strong intrinsic piezoelectricity of blue-phosphorus-like group-IV monochalcogenides, Nano Res. **15**, 209 (2021).

[54] A. Rezavand and N. Ghobadi, Stacking-dependent Rashba spin splitting in Janus bilayer transition metal dichalcogenides: The role of in-plane strain and out-of-plane electric field, Physica E **132**, 114768 (2021).

[55] A. Rezavand and Nayereh Ghobadi, Tuning the Rashba spin splitting in Janus MoSeTe and WSeTe van der Waals heterostructures by vertical strain, J. Magn. Magn. Mater. **544**, 168721 (2022).

[56] Q. F. Yao, J. Cai, W. Y. Tong, S. J. Gong, J. Q. Wang, X. Wan, C. G. Duan, and J. H. Chu, Manipulation of

the large Rashba spin splitting in polar two-dimensional transition-metal dichalcogenides, Phys. Rev. B **95**, 165401 (2017).

[57] M. N. Blonsky, H. L. Zhuang, A. K. Singh, and R. G. Hennig, *Ab initio* prediction of piezoelectricity in two-dimensional materials, ACS Nano **9**, 9885 (2015).

[58] F. Mouhat and F. X. Coudert, Necessary and sufficient elastic stability conditions in various crystal systems, Phys. Rev. B **90**, 224104 (2014).

[59] R. Bechmann, Elastic and piezoelectric constants of alpha-quartz, Phys. Rev. **110**, 1060 (1958).

[60] C. M. Lueng, H. L. W. Chan, C. Surya, and C. L. Choy, Piezoelectric coefficient of aluminum nitride and gallium nitride, J. Appl. Phys. **88**, 5360 (2000).

[61] K. A. N. Duerloo, M. T. Ong, and E. J. Reed, Intrinsic piezoelectricity in two-dimensional materials, J. Phys. Chem. Lett. **3**, 2871 (2012).

[62] W. Li and J. Li, Piezoelectricity in two-dimensional group-III monochalcogenides, Nano Res. **8**, 3796 (2015).

[63] L. Dong, J. Lou, and V. B. Shenoy, Large in-plane and vertical piezoelectricity in Janus transition metal dichalchogenides, ACS nano **11**, 8242 (2017).

[64] Y. Cui, L. Peng, L. Sun, M. Li, X. Zhang, and Y. Huang, Structures, stabilities and piezoelectric properties of Janus gallium oxides and chalcogenides monolayers, J. Phys.: Condens. Matter **32**, 08LT01 (2020).

[65] R. Hinchet, U. Khan, C. Falconi, and S.-W. Kim, Piezoelectric properties in two-dimensional materials: Simulations and experiments, Mater. Today **21**, 611 (2018).

[66] F. Li, T. Shen, C. Wang, Y. Zhang, J. Qi, and H. Zhang, Recent advances in strain-induced piezoelectric and piezoresistive effect-engineered 2D semiconductors for adaptive electronics and optoelectronics, Nano-Micro Lett. **12**, 106 (2020).

[67] D. Dimple, N. Jena, A. Rawat, R. Ahammed, M. K. Mohanta, and A. De Sarkar, Emergence of high piezoelectricity along with robust electron mobility in Janus structures in semiconducting Group IVB dichalcogenide monolayers, J. Mater. Chem. A **6**, 24885 (2018).